

CO $J=1-0$ and $J=2-1$ Line Observations of the Molecular Cloud - Blocked Supernova Remnant 3C434.1

Il-Gyo Jeong¹, Bon-Chul Koo¹, Wan-Kee Cho¹, Carsten Kramer², Jürgen Stutzki³,
Do-Young Byun^{4,5}

ABSTRACT

We present the results of CO emission line observations toward the semicircular Galactic supernova remnant (SNR) 3C434.1 (G94.0+1.0). We mapped an area covering the whole SNR in the $^{12}\text{CO } J = 1-0$ emission line using the Seoul Radio Astronomy Observatory (SRAO) 6-m telescope, and found a large molecular cloud superposed on the faint western part of the SNR. The cloud was elongated along the north-south direction and showed a very good spatial correlation with the radio features of the SNR. We carried out $^{12}\text{CO } J = 2-1$ line observations of this cloud using the Kölner Observatorium für Sub-Millimeter Astronomie (KOSMA) 3-m telescope and found a region in which the $^{12}\text{CO } J = 2-1$ to $J = 1-0$ ratio was high (~ 1.6). This higher excitation, together with the morphological relation, strongly suggested that the molecular cloud was interacting with the SNR. The systemic velocity of the molecular cloud (-13 km s^{-1}) gave a kinematic distance of 3.0 kpc to the SNR-molecular cloud system. We derived the physical parameters of the SNR based on this new distance. We examined the variation of the radio spectral index over the remnant and found that it was flatter in the western part, wherein the SNR was interacting with the molecular cloud. We therefore propose that 3C434.1 is the remnant of a supernova explosion that occurred just outside the boundary of a relatively thin, sheetlike molecular cloud. We present a hydrodynamic model showing that its asymmetric radio morphology can result from its interaction with this blocking molecular cloud.

Subject headings: ISM: individual (3C434.1) — ISM: kinematics and dynamics — ISM: molecules — radio lines: ISM — supernova remnants

1. Introduction

Supernova remnants (SNRs) appear usually spherical when they are young. Historical SNRs such as Cassiopeia A, Tycho, and Kepler are good examples. As they evolve, however, their mor-

phology can deviate considerably from sphericity by their interaction with the ambient medium. If the SNR encounters, for example, a dense molecular cloud, the SNR shell becomes distorted. In contrast, if the remnant crosses a diffuse bubble, then part of the SNR shell could blow out or could even be completely missing. Therefore, from the morphology of SNRs, we can infer their environments, which are often useful for understanding the nature and evolution of SNRs.

The SNR 3C434.1 (G94.0+1.0) is a shell-like supernova remnant with a distinct morphology in radio (Willis 1973; Goss et al. 1984; Landecker et al. 1985; Foster 2005; see Fig. 1). It has a bright eastern hemisphere which has a well-defined, circular boundary. The limb brightening indicates that we are seeing the eastern half of a spherical shell with

¹Astronomy Program, Department of Physics and Astronomy, Seoul National University, Seoul 151-742, Republic of Korea; igjeong@astro.snu.ac.kr, koo@astro.snu.ac.kr

²Instituto Radioastronomia Milimetrica (IRAM), Av. Divina Pastora 7, E-18012 Granada, Spain

³I. Physikalisches Institut, Universität zu Köln, Zùlpicher Straße 77, 50937 Köln, Germany

⁴Korea Astronomy & Space Science Institute, Daejeon 305-348, Republic of Korea

⁵Yonsei University Observatory, Yonsei University, Seongsan-ro 262, Seodaemun, Seoul 120-749, Republic of Korea

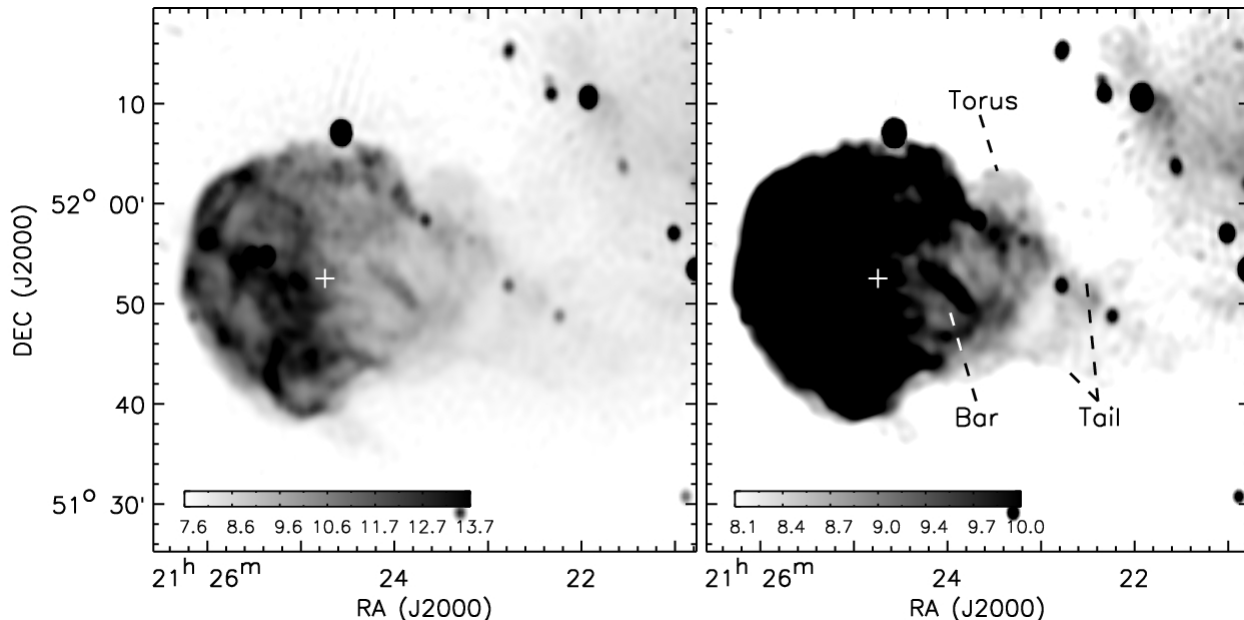


Fig. 1.— Radio continuum image of 3C434.1 at 1420 MHz from the Canadian Galactic Plane Survey data (Taylor et al. 2003). The two frames show the same image with different gray scales to emphasize the detailed radio continuum structure. The central white cross represents the geometrical center of the remnant. The features discussed in the text are labeled.

a radius of $13'$. The complex filaments projected inside the remnant implies that the shell is not uniform. The circular shell-like structure continues a little further to the west, but then the morphology becomes quite complex. Some noticeable features are as follows: (i) a linear, convergent, thin “tail” that originates out from the western end of the shell and extends much further ($\sim 20'$) to the west, (ii) a “torus” that appears to be composed of several ring structures surrounding the connecting portion of the tail and the SNR shell, and (iii) a $8'$ -long “bar” that is located near the center of the torus and extends roughly parallel to the tail. We discuss these features later in this paper.

Foster et al. (2004) explored the atomic environment of the SNR using Canadian Galactic Plane Survey (CGPS) HI 21 cm-line data. They noted fragmented HI filaments along the SNR boundary and interpreted them as parts of pre-existing stellar wind bubble produced by the massive progenitor of the SNR. They developed a dynamical model for the SNR and its wind bubble based on this scenario. The kinematic distance to the HI filaments (10 kpc), however, yielded unreasonable

parameters, and thus, they instead adopted the distance to the Perseus spiral arm (5.2 kpc) as the distance to the SNR. Later, Foster (2005) carried out follow-up multiwavelength studies in radio to X-rays. He analyzed the archival ROSAT X-ray data to show that the X-ray emission is bright and centrally-brightened in the eastern part of the SNR and that the X-ray spectrum can be fitted with a single-temperature thermal plasma model. The derived temperature and density of the X-ray emitting plasma were 4.5×10^6 K and 0.2 cm^{-3} , respectively, with a revised distance of 4.5 ± 0.5 kpc. He also detected $H\alpha$ emission correlated with the radio structure along the southeastern boundary of the SNR.

In this paper, we present the results of our CO study of 3C434.1 which gives a picture of the SNR significantly different from the previous HI studies. We found a large molecular cloud in contact with the western boundary of the SNR. The cloud was originally identified by Huang & Thaddeus (1986) in their low-resolution ($\sim 30'$) CO survey of SNRs; however, no follow-up studies have been made. We present strong evidence for the interaction of the

SNR with the molecular cloud, and we argue that the western part of the SNR is faint and complicated because the remnant is interacting with the cloud there. We derive the physical parameters of 3C434.1 based on the new kinematic distance (3 kpc) and discuss the variation of radio spectral index and the origin of the distinct radio features.

2. Observations

$^{12}\text{CO } J = 1-0$ (115.2712 GHz) observations were carried out from November 2003 to December 2003 using the Seoul Radio Astronomy Observatory (SRAO) 6-m telescope. The FWHM beam size at 100 GHz was $120''$ and its main beam efficiency was 70% (Koo et al. 2003). We used a 100 GHz SIS mixer receiver with single-side band filter and a 1024-channel auto-correlator with a 50 MHz bandwidth for front-end and back-end, respectively.

We mapped the $41' \times 39'$ (R.A. \times Dec.) area centered at $(21^{\text{h}}24^{\text{m}}50^{\text{s}}, 51^{\circ}53'00'')$ with $1'$ grid spacing by using the position switching mode. The velocity coverage was from -95 to $+35 \text{ km s}^{-1}$. The off-position was located at $(21^{\text{h}}22^{\text{m}}28^{\text{s}}, 51^{\circ}40'00'')$. The system temperature ranged from 500 to 800 K depending on the elevation and weather condition. The typical rms noise level was $\sim 0.3 \text{ K}$ at 0.5 km s^{-1} resolution. Each spectrum was integrated over 30 s. The relative calibration accuracy had been checked by observing bright standard sources near the target every one or two hours. Pointing accuracy was better than $20''$.

$^{12}\text{CO } J = 2-1$ (230.5380 GHz) follow-up line observations were performed in December 2004 using the 3-m telescope at the Kölner Observatorium für Sub-Millimeter Astronomie (KOSMA). We used a dual-channel SIS receiver (Graf et al. 1998) and acousto-optical spectrometers (Schieder et al. 1989) for front-end and back-end, respectively. The beam width and main beam efficiency were $130''$ and 68%, respectively. Pointing accuracy was better than $10''$. We have mapped an area of $20' \times 37'$ using the position-switched on-the-fly (OTF) mode with a grid spacing of $50''$. The OFF position was $(21^{\text{h}}35^{\text{m}}39^{\text{s}}.1, 52^{\circ}42'59'')$. The velocity resolutions was 0.2 km s^{-1} and the typical rms noise level was $\sim 0.3 \text{ K}$.

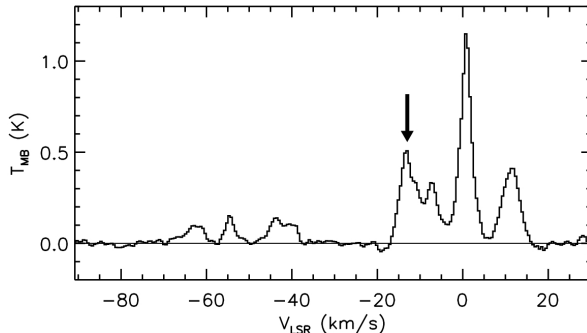


Fig. 2.— SRAO $^{12}\text{CO } J = 1-0$ average spectrum of 3C434.1. The arrow marks the -13 km s^{-1} component associated with the SNR.

The data were reduced by using CLASS¹ software, which is part of the Gildas package for single-dish spectral line analysis developed by Grenoble and IRAM. Usually the baseline was fitted with a second-order polynomial, but for some spectra we used a third-order polynomial too.

3. Results

3.1. SRAO $^{12}\text{CO } J = 1-0$

Several molecular clouds are detected in the velocity range covered by our observations. Figure 2 shows the average spectrum of the area: several velocity components are apparent; bright components between -20 and $+20 \text{ km s}^{-1}$ and faint components between -70 and -35 km s^{-1} .

Figure 3 shows the channel maps of the prominent velocity components. The components at large negative velocities ($-70 \sim -35 \text{ km s}^{-1}$) are located outside the remnant; the -44 km s^{-1} cloud is located a few arc minutes beyond the southeast boundary. The -55 and -61 km s^{-1} molecular clouds are located close to the SNR boundary, but their intensities are very weak and line widths are narrow. Thus, we consider it unlikely, that these features have any relation with the remnant. The positive velocity ($v_{\text{LSR}} \geq 0 \text{ km s}^{-1}$) components are associated with the complex local clouds of Cep OB2 and Cyg OB7 at 0.8 kpc (Humphreys 1978). These clouds are located in the southern part of the field, and we do not find any correlated features with the radio continuum emission.

¹<http://www.iram.fr/IRAMFR/GILDAS>

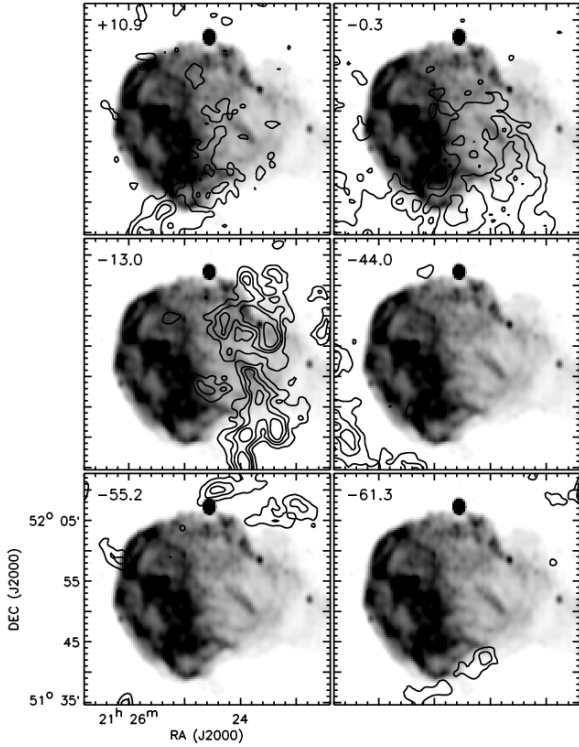


Fig. 3.— SRAO $^{12}\text{CO } J = 1-0$ contoured channel maps of prominent velocity components. Individual frames show single channel maps of width = 0.5 km s^{-1} . Velocity centers are marked at the top left corners. The contour levels are 0.9, 2, 3, and 4.5 K in brightness temperature. The gray-scale image in each channel map is the CGPS 1420 MHz radio continuum image of 3C434.1.

It is the -13 km s^{-1} cloud that shows a clear spatial correlation with the radio continuum emission. The cloud is widely distributed over the western part of the remnant where the radio continuum intensity is low. Figure 4 compares the distributions of the CO and radio continuum intensities in detail from $v_{\text{LSR}} = -9.8$ to -15.8 km s^{-1} . The cloud is elongated vertically along the western boundary of the remnant. At -11.8 to -12.8 km s^{-1} , the southern part of the cloud is bright and there is a thin filamentary structure that matches well with the western boundary of the torus structure in the radio continuum. The bright CO region matches well with the southern curved edge of the radio continuum. At -12.8 to -13.8 km s^{-1} , the northern and southern parts of the

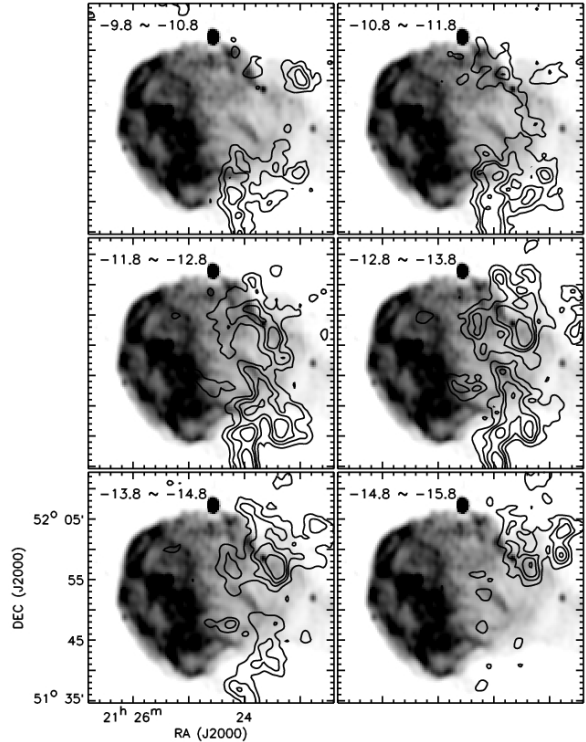


Fig. 4.— Detailed SRAO $^{12}\text{CO } J = 1-0$ channel maps of 3C434.1 from -10.0 to -15.6 km s^{-1} . Each frame shows intensity distributions averaged over two channels or 1.0 km s^{-1} . Contour levels are 0.9, 2, 3 and 4.5 K in brightness temperature. The Gray-scale is the CGPS 1420 MHz radio continuum image.

cloud are about equally bright and there is emission along the bar structure in the radio continuum.

The above morphological correlation between the CO and radio continuum strongly suggests that the CO cloud is interacting with the SNR and that the complex radio morphology of the SNR is caused by this interaction. We estimate the mass of the western molecular cloud by integrating the CO emission over $v_{\text{LSR}} = -8$ to -18 km s^{-1} in an area of $23' \times 39'$ and assuming a Galactic CO-to- H_2 conversion factor of $2.3 \times 10^{20} \text{ cm}^{-2} (\text{K km s}^{-1})^{-1}$ (Strong et al. 1988). The resulting mass is $(1.00 \pm 0.02) \times 10^4 d_3^2 M_{\odot}$ where d_3 is the distance to the SNR normalized to 3 kpc (see § 4.1) and the error is 1σ rms error.

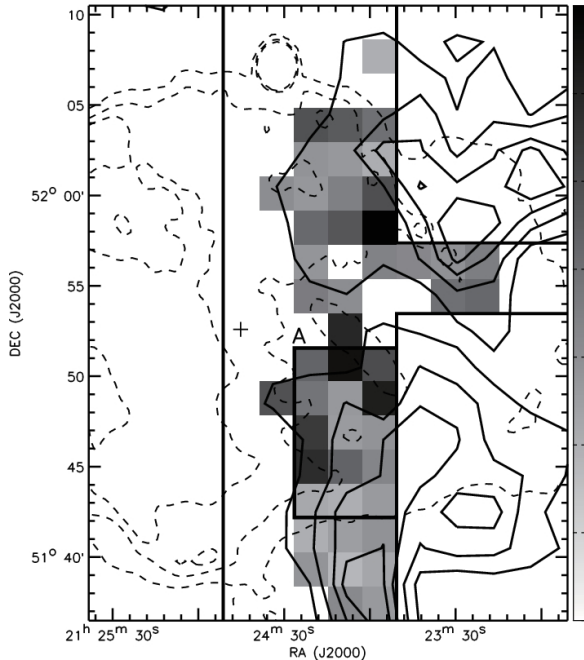


Fig. 5.— $^{12}\text{CO } J = 2-1/1-0$ ratio map in gray scale. The gray scale varies linearly from 0.1 to 1.8 with the darker scale for the higher ratios. The dashed contours represent the 1420 MHz radio continuum emission of the SNR (contour levels: 8.2, 10, and 12 K in brightness temperature). The solid contour is the SRAO $^{12}\text{CO } J = 1-0$ integrated intensity map from $v_{\text{LSR}} = -16$ to -8 km s^{-1} (levels: 4, 8, 12, 15×1 K km s^{-1}). The bold line marks the area observed with KOSMA $^{12}\text{CO } J = 2-1$.

3.2. KOSMA $^{12}\text{CO } J = 2-1$

A high $^{12}\text{CO } J = 2-1/1-0$ ratio identifies shocked warm and dense CO gas. Figure 5 shows the spatial variation of the $^{12}\text{CO } J = 2-1/1-0$ ratio obtained from the SRAO $^{12}\text{CO } J = 1-0$ and KOSMA $^{12}\text{CO } J = 2-1$ maps integrated over $v_{\text{LSR}} = -16$ to -8 km s^{-1} and binned to $2' \times 2'$. We exclude pixels with an integrated intensity less than 2.5 K km s^{-1} in order to exclude positions with low S/N ratios from the map. In Figure 5, high (≥ 1.0) ratios are found toward the southern molecular cloud. The spectra of this area are shown in Figure 6. Note that the 0 km s^{-1} component shows $J = 2-1$ emission weaker than the $J = 1-0$ emission with $^{12}\text{CO } J=2-1/J=1-0$ ratio of 0.3 to 1.0 which is typical for giant molec-

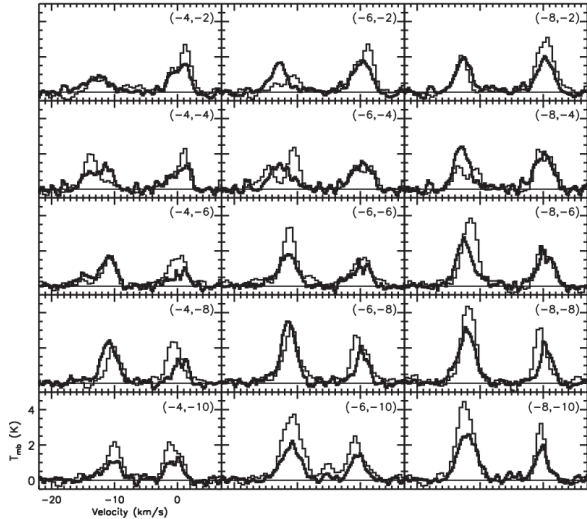


Fig. 6.— CO molecular line spectra of SRAO $J = 1-0$ (thin lines) and KOSMA $J = 2-1$ (thick lines) at region A of Fig. 5. The positions of the spectra are marked in each frame as coordinates relative to the geometrical center of the remnant, ($21^{\text{h}}24^{\text{m}}45^{\text{s}}$, $51^{\circ}52'27''$).

ular clouds (Sakamoto et al. 1994). The position $(-4, -10)$ also shows an example of ordinary CO line profiles of unshocked molecular clouds between -16 and -8 km s^{-1} . Here, the ratio is 0.5 at a velocity of -11 km s^{-1} . On the other hand, the -13 km s^{-1} component has a higher $J=2-1/J=1-0$ ratio. The $^{12}\text{CO } J=2-1/J=1-0$ integrated intensity ratio varies from 0.5 to 1.6 in region A in Figure 5 and the highest value (1.6) is at ($21^{\text{h}}24^{\text{m}}8^{\text{s}}$, $51^{\circ}50'30''$) or at $(-6, -2)$ in Figure 6. Typically, the high ratio regions are located at the boundary of the southern molecular clouds with the peak velocity of -13 km s^{-1} . However, at position $(-4, -4)$, only the -11 km s^{-1} velocity component shows the high ratio CO line emissions. The ratio is 0.95 at this position using CO integrated intensity results.

A ratio higher than ~ 1 indicates the presence of warm and dense CO gas, presumably heated and compressed by the SNR shock (e.g., Koo et al. 2001). We use the large velocity gradient (LVG) model (Scoville & Solomon 1974; Goldreich & Kwan 1974) to estimate the physical parameters of the shocked gas. Using $T_{mb, J=1-0} = 0.5$ K and $^{12}\text{R}_{2-1/1-0} = 1.6$ at the $(-6, -2)$ posi-

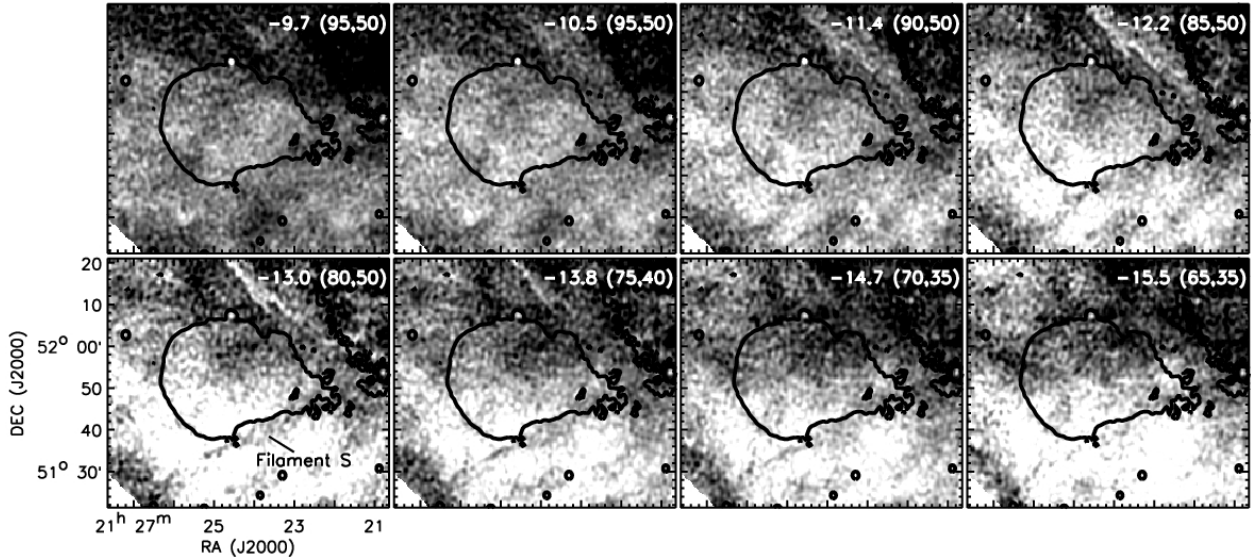


Fig. 7.— CGPS HI distribution of 3C434.1 from -9.7 to -15.5 km s^{-1} at 0.8 km s^{-1} separation. The gray scales are different for individual frames, and the maximum and minimum brightness temperatures of the scales (in Kelvins) are marked in individual frames in parentheses. The contour is the CGPS 1420 MHz radio continuum contour at 8 K.

tion, we obtain $n(\text{H}_2) \sim 2.0 \times 10^3 \text{ cm}^{-3}$ and $X(^{12}\text{CO})/(dv/dr) \sim 7.9 \times 10^{-8} \text{ pc (km s}^{-1})^{-1}$ for $T_k = 100$ K where $X(^{12}\text{CO})/(dv/dr)$ is the fractional abundance of ^{12}CO relative to H_2 [$X(^{12}\text{CO})$] per unit velocity gradient interval. This gives a CO column density of $2.4 \times 10^{15} \text{ cm}^{-2}$ assuming a velocity width of $\Delta v = 5 \text{ km s}^{-1}$. This is valid when the emitting region fills the telescope beam (FWHM= $130''$). If the beam filling factor is lower, e.g., ~ 0.1 , the source intrinsic brightnesses and the column density derived scale up by the inverse factor, i.e. by ~ 10 , whereas the density, derived from the line ratio, stays roughly the same.

4. Discussion

4.1. New Distance to 3C434.1 and Its Physical Parameters

The morphological relation and the high $^{12}\text{R}_{2-1/1-0}$ ratio strongly suggest that the SNR 3C434.1 is interacting with the molecular cloud that shows CO emission at -13 km s^{-1} . The kinematic distance corresponding to -13 km s^{-1} is 3.0 kpc assuming the Galactic rotation curve of Brand & Blitz (1993) with $R_0 = 8.5$ kpc and $v_0 = 220 \text{ km s}^{-1}$.

Our kinematic distance is less than the 4.5 ± 0.9 kpc distance proposed by Foster (2005).

Foster et al. (2004) noted fragmented HI filaments along the SNR boundary at -80 km s^{-1} and interpreted them as parts of a preexisting stellar wind bubble produced by the massive progenitor of the SNR. According to our result, however, the velocity difference is too large for this component to be associated with the SNR. We instead examine the correlation of the HI emission at around $v_{\text{LSR}} = -13 \text{ km s}^{-1}$ with the SNR. Figure 7 shows the CGPS HI channel maps from -9.7 to -15.5 km s^{-1} . We first note that there is a large-scale gradient in HI intensity over the field: The northwestern area is brighter than the southeastern area. Second, there is a large filamentary HI-absorption structure in the northwestern area of the field, but it is not related to the SNR. Absorption from the -13 km s^{-1} cloud interacting with the SNR is not apparent. Third, there is a long, linear HI structure just outside of, and along, the southern SNR boundary at velocities from -11 to -15 km s^{-1} (labelled "Filament S"). The radio brightness drops sharply across the HI filament. Therefore, the linearly-shaped southwestern radio boundary seems to be related to this HI structure.

Table 1: Physical parameters of SNR 3C434.1

Parameter	Value
Distance (kpc)	3.0
Radius of eastern shell (pc)	11.3
Age (yr)	7,900
Ambient hydrogen density (cm^{-3})	0.19
SN energy (ergs)	0.19×10^{51}
H ₂ mass of interacting molecular cloud (M_{\odot})	1.0×10^4

The geometrical center of the shell is ($21^{\text{h}} 24^{\text{m}} 45^{\text{s}}$, $51^{\circ} 52' 27''$) and its radius (R_s) is $13'$ or 11.3 pc at 3.0 kpc. The spherical morphology suggests that we can apply standard model to this part of the remnant, as has been confirmed by hydrodynamic simulations (e.g., Tenorio-Tagle et al. 1985). From the ROSAT X-ray spectra, Foster (2005) derived an electron temperature of $T_e = 4.5 \times 10^6$ K for the host X-ray emitting gas, which corresponds to a shock speed $v_s = (16k_B T_e / 3\mu)^{1/2} = 570$ km s^{-1} (where $\mu = 1.4m_{\text{H}}/2.3 = 0.61m_{\text{H}}$ is the mean mass per particle, $m_{\text{H}} =$ mass of H nuclei, and k_B is Boltzmann's constant). This speed is large and we may assume that the SNR is in its adiabatic phase. Then, from the Sedov solution, the radius and the velocity give an age of $0.4R_s/v_s = 7,900$ yr. The estimated volume emission measure is $\int n_e^2 dV = 4.5 \times 10^{57} \text{ cm}^{-6} \text{ pc}^3$ (scaled to 3.0 kpc). Foster (2005) assumed that this X-ray emission comes from a thin shell in contact with the stellar wind bubble. We instead assume that the X-ray emitting gas is roughly filling the eastern half because the X-ray emission is centrally brightened, which gives an rms electron density of 0.23 cm^{-3} . Then the SN explosion energy is, from the Sedov solution, $E_{SN} = 2.1 \times 10^{51} n_0 (R/10 \text{ pc})^3 (v_s/10^3 \text{ km s}^{-1})^2 = 0.19 \times 10^{51}$ ergs, where $n_0 (= n_e/1.2) = 0.19 \text{ cm}^{-3}$ is the number density of hydrogen nuclei of the medium taking into account an He abundance of 10% by number. This is smaller than the canonical value of 10^{51} ergs but not unreasonable. The derived parameters of the SNR are summarized in Table 1. The dynamical evolution of the SNR including the western part interacting with the molecular cloud will be discussed in § 4.3.

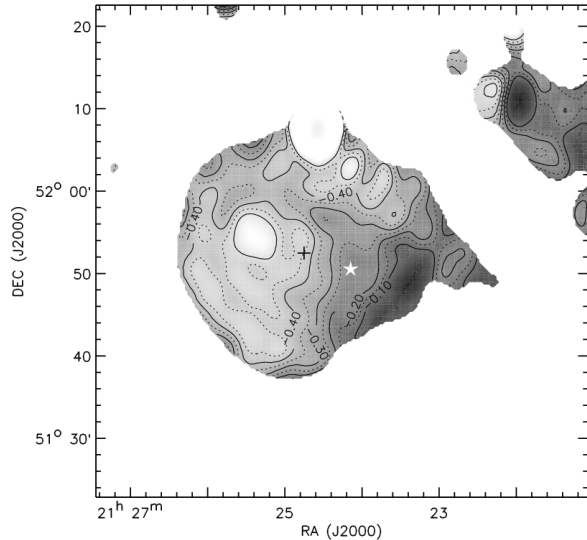


Fig. 8.— Spectral index map of 3C434.1. The spectral indices (α in $S_{\nu} \propto \nu^{\alpha}$) are derived only for the areas with 1420 and 408 MHz brightnesses larger than 1.2 K and 15.2 K corresponding to $5\text{-}\sigma$ brightnesses, respectively. The range of gray scale in α is from -0.6 to $+0.2$. The solid contours are drawn every 0.1 while the dotted contours are drawn every 0.05 . The star symbol shows the location of the high CO ratio region.

4.2. Variation of Radio Spectral Index

SNRs interacting with molecular clouds often show flattening or a turnover of the radio synchrotron spectrum at low frequencies around the areas of the interaction, i.e., the spectral index becomes larger than the typical value ($\alpha \sim -0.5$; $S_{\nu} \propto \nu^{\alpha}$) of shell-type SNRs or even becomes positive. Some examples are IC 443 (Green 1986), the Cygnus Loop (Leahy & Roger 1998), HB 21 (Koo et al. 2001; Leahy 2006), 3C391 (Brogan et al. 2005), and W44 (Castelletti et al. 2007). Several mechanisms have been proposed for the flat radio spectrum: free-free absorption by thermal plasma in the dense postshock region, ionization losses from mixed dense molecular material, second-order Fermi acceleration by the turbulent medium in the postshock region (Leahy & Roger 1998; Ostrowski 1999), the higher compression ratio owing to the energy loss to cosmic ray particles (Bykov et al. 2000), and the relatively flat spectrum of ambient cosmic rays entering the shock

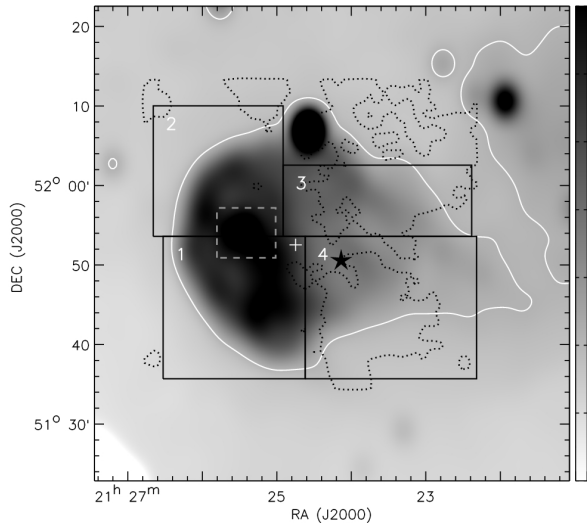


Fig. 9.— Convolved 1420 MHz radio continuum image of 3C434.1. The Gray scale varies linearly from 6 to 13 K with the darker scale for the higher temperatures. Boxes show the regions for the $T - T$ plots in Fig. 10. The dashed box represents the area excluded in the $T - T$ plots. The star symbol shows the location with high CO $J = 2 - 1/1 - 0$ ratio.

(Chevalier 1999). For 3C434.1, Foster et al. (2004) derived a spectral index of -0.38 ± 0.03 from 150 MHz to 2.7 GHz and noted that the western extension has a slightly flatter spectrum (≤ 0.3) than the eastern radio shell. Later Kothes et al. (2006) derived a somewhat steeper index of -0.48 ± 0.02 by fitting the total fluxes from 30 MHz to 5 GHz.

We produce a spectral index map using the CGPS 1420 and 408 MHz radio continuum data. We first convolve the 1420 MHz image (FWHM=49") to the beam size (168") of the 408 MHz image, and we subtract a constant background in each image: 7.3 and 77 K for 1420 and 408 MHz, respectively. The resulting spectral index map is shown in Figure 8, which confirms the flat spectrum in the western area: The eastern bright area has an index of -0.45 to -0.3 whereas the southwestern area has -0.1 to 0.0 . The area around ($21^{\text{h}} 23^{\text{m}} 20^{\text{s}}$, $51^{\circ} 49' 10''$) has a particular flat spectrum (~ 0.0). The average spectral index of the entire SNR is -0.33 .

We also derive the spectral index using the “ $T-T$ plot method”, wherein we make a pixel-to-

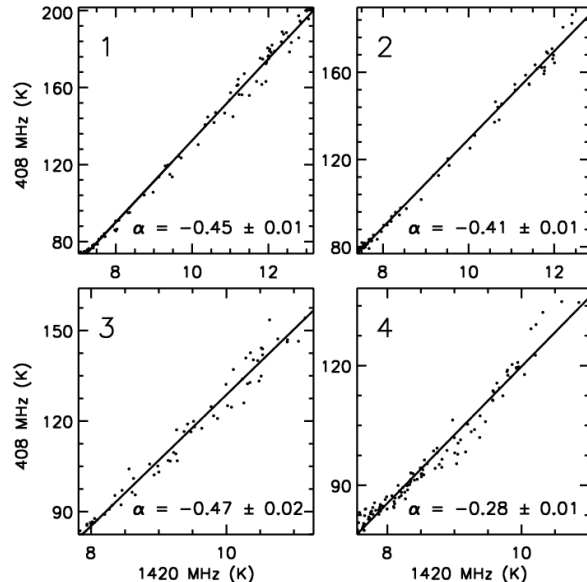


Fig. 10.— $T - T$ plot results of four regions obtained by pixel-to-pixel comparison of CGPS 408 and 1420 MHz radio continuum images.

pixel comparison of the brightness temperatures at two different frequencies and derive the slope. The advantage of this method is that the slope is not affected by potentially different zero levels of each set of frequency data and smooth background emission (Turtle et al. 1962). We divide the target area into four regions and derive the index in each region from 1420 and 408 MHz data. Figure 9 shows the boundary of the four regions in the convolved 1420 MHz radio continuum image, and Figure 10 shows their pixel-to-pixel comparison of the brightness at two frequencies, respectively. The indices derived from least-squares fitting are given in the individual graphs. In three regions, the index varies little (-0.47 to -0.41), but in the southwestern area (region 4), the index is -0.28 ± 0.01 which is considerably flatter than the other regions. This flat spectral index could be due to the interaction with the molecular cloud, confirming the reasoning given above. The average spectral index of all areas is -0.42 ± 0.01 .

4.3. Interaction with the Molecular Cloud and Radio Morphology

The dynamical evolution of a SNR originating near the boundary of a dense molecular cloud has

been numerically studied by several authors (e.g., Tenorio-Tagle et al. 1985; Wang et al. 1992; Ferreira & de Jager 2008). The details of the evolution depend on the physical and geometrical parameters of the simulation, e.g., the SN explosion energy, the densities of the molecular cloud and diffuse gas, the location of SN explosion site, etc. If the SN explodes in the diffuse medium close to the boundary of the molecular cloud, the SN blast wave expands adiabatically until it encounters the cloud. When the blast wave hits the dense cloud, two waves are produced: a shock wave propagating into the cloud and a reflected wave propagating back to the interior of the SNR. The propagating shock wave decelerates rapidly because of the high density and also because the reflective wave lowers the driving pressure near the cloud. Because the molecular cloud’s density is considerably larger than that of the diffuse medium, it is not overly disrupted, and the SNR appears as a semicircular shell. The semicircular morphology of the SNR CTB 109, which is another SNR blocked by a molecular cloud (Tatematsu et al. 1987, 1990; Sasaki et al. 2006), has been acceptably explained by this scenario (Wang et al. 1992).

The SNR 3C434.1 also has a semicircular shape, but it does not quite fit into the above scenario: It has a narrow, convergent tail that originates from the western end of the shell and extends much further ($> 25'$ from the center) to the west. Also, there is a torus that appears to surround the western end of the tail. The inner boundary of the torus is quite circular with a clear limb brightening. This probably indicates that the cloud that is interacting with 3C434.1 is thin and that the blast wave has broken through it. This hypothesis is consistent with the presence of an elongated CO cloud along the western boundary of the SNR.

We have developed a hydrodynamic model to confirm the above hypothesis. We assume that the SN explodes at 1 pc from the boundary of a sheetlike cloud that has a thickness of 5 pc. The H-nuclei number density of the cloud is assumed to be 20 cm^{-3} , which is a typical density for the interclump medium of giant molecular clouds (e.g. Chevalier 1999, and references therein). For the density of the diffuse medium and SN explosion energy, we adopt 1 cm^{-3} and 10^{51} ergs, respectively. These canonical values are both about 5 times larger than those of 3C434.1 but since the

radius (and velocity) scales with $(E_{SN}/n)^{0.2}$ in the Sedov phase, the resulting morphological evolution in time should be approximately correct. The density distribution of a core-collapse SN is characterized by a central region of approximately constant density and an outer region with a steep gradient (e.g., Matzner & McKee 1999). We assume that the SN ejecta, which are freely expanding, are composed of a central region of constant density and an outer region with a steep power law ($\rho(r) \propto r^{-9}$) with a total mass of $8 M_{\odot}$. When the steep power-law portion of the ejecta is interacting with the ambient medium, a similarity solution exists (Chevalier 1982). Our numerical simulation starts at $t = 350$ yr, and the distributions of the physical parameters at this time are taken from this similarity solution. We first considered a model in which the cloud was shaped like an infinitely extended disk. This model, however, did not produce the torus-like structure in the west in time. We therefore assume that the cloud has a cylindrical hole at the center, so that the shock can penetrate through the central hole. The radius of the hole is assumed to be 3 pc. For the calculation, we adopt the three-dimensional hydrodynamic code developed by Harten, Lax and van Leer (HLL) with a modified cooling effect (Harten et al. 1983). This HLL code is efficient for describing the shock propagation. The simulation box consists of $512 \times 256 \times 256$ grid points with a spatial resolution of $1/16$ pc. We calculate one quadrant column along the symmetric axis (x -axis), and we copy the results to the other quadrants by assuming symmetry.

The results of the numerical simulations are shown in Figure 11 where we show the time evolution of the density and velocity distributions in the upper and lower panels, respectively. Figure 11 (a) shows the initial distributions at $t = 350$ yr. The ambient shock is at 1.89 pc, while the reverse shock propagating into the SN ejecta is at 1.60 pc from the explosion center. Between these two shocks, the shocked ambient medium and the shocked ejecta are separated by a contact discontinuity which is at 1.66 pc (see Chevalier 1982). At $t = 1,950$ yr (Fig. 11(b)), the SNR blast wave propagating to the right has been significantly distorted by the interaction with the cylindrical wall of the cloud. The cloud boundary has been compressed to high density while the shock propagat-

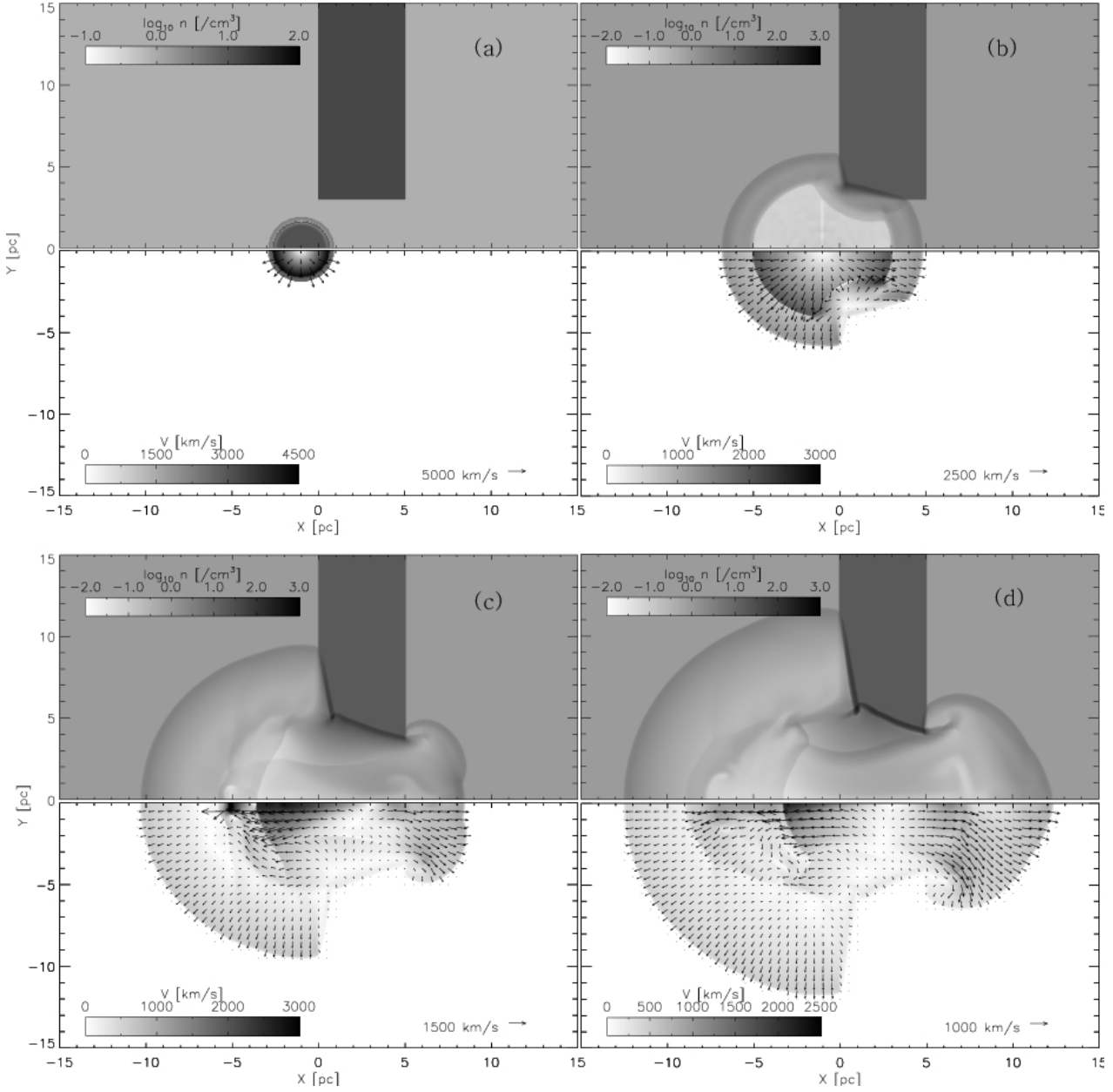


Fig. 11.— Hydrodynamic evolution model for 3C434.1. Frames from (a) to (d) show the density (upper panels) and velocity structures (lower) at different stages in the SNR evolution ($t = 350, 1950, 4950$ and 7950 yr, respectively). In the density panels, the color bars are shown in logarithmic units. In the velocity panels, arrows mark both the direction as well as the magnitude of the velocity field. The molecular cloud with a cylindrical hole of radius 3 pc is shown in dark gray on the density panel, but the molecular cloud and intercloud medium cannot be seen separately in the velocity panel, because their velocity distribution is assumed to be static.

ing into the dense cloud is considerably decelerated. Note that the reverse shock in the interact-

ing region is now propagating backward into the central area in the rest frame, whereas the reverse

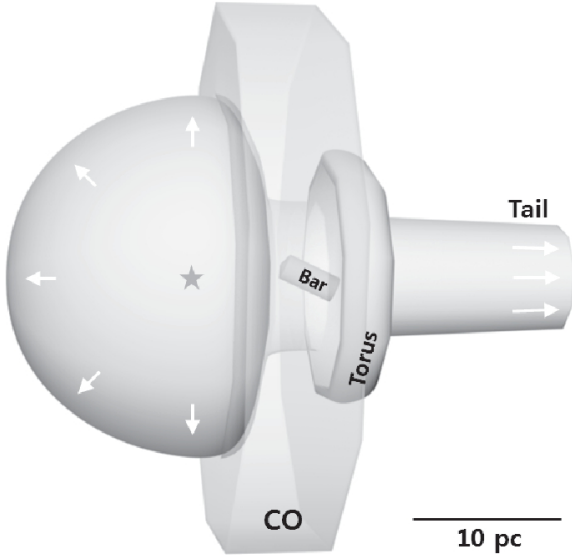


Fig. 12.— Schematic diagram of the SNR 3C434.1. The thin, disklike molecular cloud interacting with the SNR is labeled “CO”. The pronounced radio continuum features (torus, bar, and tail) are also labeled. The asterisk symbol marks the position of the SN explosion.

shocks in the other regions are still propagating forward in the rest frame. At $t = 4,950$ yr (Fig. 11(c)), the radius of the left-half of the SNR becomes 9.4 pc, which is close to that of the Sedov solution, as expected. Meanwhile, the blast wave propagating to the right has propagated through the cylindrical hole and popped out of the cloud producing a mushroom-like structure. In the interior, the reverse shocks from the side walls collide and produce a fast flow to the east. At $t = 7,950$ yr (Fig. 11(d)), which is close to the age of 3C434.1, again the radius of the left-half of the SNR agrees with that (11.3 pc) of the Sedov solution. The blast wave on the right by now appears almost spherical. Note that the velocity of the blast wave on the right is larger than on the left, so that the distance to the rightmost front from the explosion center is more than 13 pc. The density and velocity distributions in the interior of the SNR become complex owing to the collision of waves and hydrodynamic instabilities. Meanwhile, the shock propagating into the dense cloud became partially radiative, so that the density of the shocked cloud is very high ($\sim 10^3 \text{ cm}^{-3}$).

The resulting morphology of the numerical simulation is close to the radio morphology of 3C434.1 but there are some differences. In Figure 12, we draw a schematic diagram of 3C434.1 including its radio-continuum features, i.e., torus, bar, and tail. The spherical eastern half of the SNR with a radius of 11 pc is quite consistent with the hydrodynamic model. The torus structure partly matches the mushroom structure in the model. The shocked, highly-compressed boundary of the molecular cloud corresponds to the northwestern SNR boundary with enhanced radio brightness in the radio map. The bar structure represents the dense swept-up cloud material embedded within the SNR. The long, radio-continuum tail that extends much further than the overall radius of the SNR, however, is not easy to explain. It seems to indicate that there might have been a preexisting tunnel of much lower density in the ISM. An interesting possibility would be a “star trail” as in the Crab Nebula (Blandford et al. 1983; Cox et al. 1991). In the Crab nebula, there is a thin (~ 0.5 pc) jetlike structure in the radio continuum to the north, and it was attributed to the trail of the progenitor star; the progenitor star was moving before the explosion and its red supergiant wind leaves a trail through which the SN blast wave can propagate beyond. In 3C434.1, the radius of the tail is wide, i.e., $5'$ or ~ 4.4 pc just behind the torus. However, if the trail is filled with hot, shocked gas, the trail will expand sideways at about the velocity of the sound speed of the hot gas, which is 250 km s^{-1} for 4.5×10^6 K X-ray emitting gas, the maximum increment of the radius of the tunnel by the SNR would be < 2 pc. Therefore, the tunnel might have had a large radius initially.

5. Conclusion

We observed $^{12}\text{CO } J = 1-0$ and $J = 2-1$ emission lines toward the SNR G94.0+1.0 (3C434.1) using the SRAO and KOSMA telescopes. The presence of a molecular clouds around the SNR had been known from the previous low-resolution ($30'$) survey, but the relation between the two had not been investigated. Our observations reveal a thin molecular cloud elongated along the north-south direction superposed on the western part of the SNR. The spatial correlation of the CO emission with the radio continuum structure together with its high $^{12}\text{CO } J = 2-1/1-0$ line ratio

strongly suggests that the cloud is interacting with the SNR. The relatively flat radio spectral index may also be due to the interaction. The systemic velocity of the cloud is -13 km s^{-1} , which yields a new kinematic distance of 3 kpc to the SNR. The new distance implies that 3C434.1 is located within the Perseus spiral arm. This, together with the interaction with the molecular cloud suggests that 3C434.1 is likely a remnant of a core-collapse supernova that had a massive ($\gtrsim 8 M_{\odot}$) stars as its progenitor.

Our result indicates that the distinct radio morphology of 3C434.1 is due to the interaction with a dense, blocking cloud in the west. Indeed the spatial correlation between the CO and radio continuum features is remarkable. Features such as the torus, bar, and tail must reflect different efficiencies of particle acceleration depending on the shock speed, ambient density, and magnetic field strength. Currently, strong evidence exists for 45 SNRs, which indicates their interaction with molecular clouds according to the compilation by Jiang et al. (2010), which covers 16% of the known Galactic SNRs (see also Jeong et al. 2012). 3C434.1 is one such prototypical SNR in this category, and future high-resolution observations and hydromagnetic simulations will give us a better understanding of this intriguing SNR.

We would like to thank Chris McKee and Dave Green for helpful discussions. Numerical simulations in this paper were performed by using a high performance computing cluster in the Korea Astronomy and Space Science Institute. The KOSMA 3-m submillimeter telescope at the Gornegrat-Süd operated by the University of Cologne in collaboration with Bonn University and supported by special funding from the Land NRW. The observatory is administered by the International Foundation Gornegrat and Jungfrau-joch. This research used the facilities of the Canadian Astronomy Data Centre operated by the National Research Council of Canada with the support of the Canadian Space Agency. This work is supported by Basic Science Research program through the National Research Foundation of Korea (NRF) funded by the Ministry of Education, Science and Technology (NRF-2011-0007223).

REFERENCES

- Blandford, R. D., Kennel, C. F., McKee, C. F., & Ostriker, J. P. 1983, *Nature*, 301, 586
- Brand, J., & Blitz, L. 1993, *A&A*, 275, 67
- Brogan, C. L., Lazio, T. J., Kassim, N. E., & Dyer, K. K. 2005, *AJ*, 130, 148
- Bykov, A. M., Chevalier, R. A., Ellison, D. C., & Uvarov, Y. A. 2000, *ApJ*, 538, 203
- Castelletti, G., Dubner, G., Brogan, C., & Kassim, N. E. 2007, *A&A*, 471, 537
- Chevalier, R. A. 1982, *ApJ*, 258, 790
- Chevalier, R. A. 1999, *ApJ*, 511, 798
- Cox, C. I., Gull, S. F., & Green, D. A. 1991, *MNRAS*, 250, 750
- Ferreira, S. E. S., & de Jager, O. C. 2008, *A&A*, 478, 17
- Foster, T. 2005, *A&A*, 441, 1043
- Foster, T., Routledge, D., & Kothes, R. 2004, *A&A*, 417, 79
- Goldreich, P., & Kwan, J. 1974, *ApJ*, 189, 441
- Goss, W. M., Mantovani, F., Salter, C. J., Tomasi, P., & Velusamy, T. 1984, *A&A*, 138, 469
- Graf, U. U., Honingh, C. E., Jacobs, K., Schieder, R., & Stutzki, J. 1998, *Astronomische Gesellschaft Meeting Abstracts*, 14, 120
- Green, D. A. 1986, *MNRAS*, 221, 473
- Harten, A., Lax, P. D., & van Leer, B. 1983, *SIAMR*, 25, 35
- Huang, Y.-L., & Thaddeus, P. 1986, *ApJ*, 309, 804
- Humphreys, R. M. 1978, *ApJS*, 38, 309
- Jeong, I.-G., Byun, D.-Y., & Koo, B.-C. et al. 2012, *Ap&SS*, 342, 389
- Jiang, B., Chen, Y., & Wang, J. et al. 2010, *ApJ*, 712, 1147
- Koo, B.-C., Park, Y.-S., & Hong, S. S. et al. 2003, *J. Korean Astron. Soc.*, 36, 43

- Koo, B.-C., Rho, J., Reach, W. T., Jung, J., & Mangum, J. G. 2001, *ApJ*, 552, 175
- Kothes, R., Fedotov, K., Foster, T. J., & Uyaniker, B. 2006, *A&A*, 457, 1081
- Landecker, T. L., Higgs, L. A., & Roger, R. S. 1985, *AJ*, 90, 1082
- Leahy, D. A. 2006, *ApJ*, 647, 1125
- Leahy, D. A., & Roger, R. S. 1998, *ApJ*, 505, 784
- Matzner, C. D., & McKee, C. F. 1999, *ApJ*, 510, 379
- Ostrowski, M. 1999, *A&A*, 345, 256
- Sakamoto, S., Hayashi, M., Hasegawa, T., Handa, T., & Oka, T. 1994, *ApJ*, 425, 641
- Sasaki, M., Kothes, R., Plucinsky, P. P., Gaetz, T. J., & Brunt, C. M. 2006, *ApJ*, 642, L149
- Schieder, R., Tolls, V., & Winnewisser, G. 1989, *Exp. Astron.*, 1, 101
- Scoville, N. Z., & Solomon, P. M. 1974, *ApJ*, 187, L67
- Strong, A. W., Bloemen, J. B. G. M., & Dame, T. M. et al. 1988, *A&A*, 207, 1
- Tatematsu, K., Fukui, Y., Iwata, T., Seward, F. D., & Nakano, M. 1990, *ApJ*, 351, 157
- Tatematsu, K., Fukui, Y., & Nakano, M. et al. 1987, *A&A*, 184, 279
- Taylor, A. R., Gibson, S. J., & Peracaula, M. et al. 2003, *AJ*, 125, 3145
- Tenorio-Tagle, G., Bodenheimer, P., & Yorke, H. W. 1985, *A&A*, 145, 70
- Turtle, A. J., Pugh, J. F., Kenderdine, S., & Pauliny-Toth, I. I. K. 1962, *MNRAS*, 124, 297
- Wang, Z., Qu, Q., Luo, D., McCray, R., & Mac Low, M.-M. 1992, *ApJ*, 388, 127
- Willis, A. G. 1973, *A&A*, 26, 237